

# IOVS4NeRF: Incremental Optimal View Selection for Large-Scale NeRFs

Jingpeng Xie, Shiyu Tan, Yuanlei Wang, Yifei Xue, Yizhen Lao

**Abstract**—Neural Radiance Fields (NeRF) have recently demonstrated significant efficiency in the reconstruction of three-dimensional scenes and the synthesis of novel perspectives from a limited set of two-dimensional images. However, large-scale reconstruction using NeRF requires a substantial amount of aerial imagery for training, making it impractical in resource-constrained environments. This paper introduces an innovative incremental optimal view selection framework, IOVS4NeRF, designed to model a 3D scene within a restricted input budget. Specifically, our approach involves adding the existing training set with newly acquired samples, guided by a computed novel hybrid uncertainty of candidate views, which integrates rendering uncertainty and positional uncertainty. By selecting views that offer the highest information gain, the quality of novel view synthesis can be enhanced with minimal additional resources. Comprehensive experiments substantiate the efficiency of our model in realistic scenes, outperforming baselines and similar prior works, particularly under conditions of sparse training data.

## I. INTRODUCTION

Neural Radiance Fields(NeRFs) [1] has significantly enables the perception of 3D scenes using 2D data[2]. Compared to previous deep learning approaches [3, 4], such as those based on point clouds [5, 6], NeRF offers higher reconstruction efficiency and remarkable adaptability in different research realms. It employs an implicit MLP network to better perceive the physical world[7] and has found applications in various fields, including robotics and 3D modeling.

The original NeRF encodes scene information into network parameters and uses differentiable volume rendering, which requires substantial computational resources [8], especially for large-scale scenes, leading to inefficient reconstruction. To address these issues, previous works [9, 10, 11, 12, 13] have utilized combinations of hash functions, spherical harmonics, and both explicit and implicit scene representations to enable faster training of NeRF. Some works have also expanded NeRF reconstruction to focus on large-scale scenes [14, 15, 16, 17]. These methods mainly involve decomposing a large scene into several smaller scenes, with each small scene independently trained by a NeRF sub-module. While this approach can achieve high-fidelity reconstruction and significantly increase reconstruction speed compared to the original NeRF, it is based on the premise of using extensive resources. However, in resource-constrained situations where only a limited number of images can be used as input, the reconstruction results tend to have severe artifacts and lower visual fidelity.

Inspired by the Next-Best View (NBV) problem [18], we reduce the number of images in the dataset to minimize computational resource consumption. We aim for each image

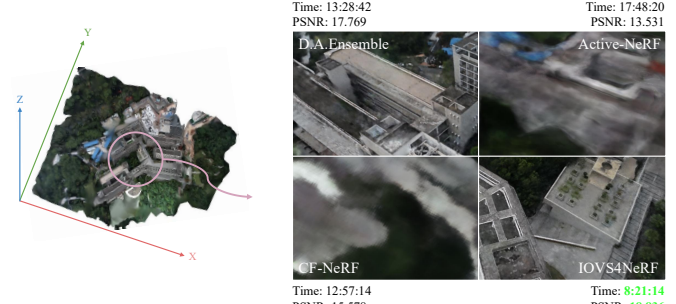


**Fig. 1: Novel View Synthesis Comparison.** We propose a new NeRF framework, and the comparison on the ArtSci dataset across four different model strategies reveals that our method outperforms others in terms of both processing time and reconstruction efficiency.

in the limited input to contain as much information as possible, meaning the dataset is composed of images with the highest information gain to maximize scene understanding. Selecting the next best viewpoint to maximize information gain typically involves using uncertainty estimation for quantification. To address the problem of training NeRF in resource-constrained scenarios, some recent works have employed uncertainty-guided NBV selection[19, 20, 21, 22]. These methods significantly modify the internal network, resulting in low reusability. Other works[23] do not make any changes to NeRF itself, offering strong generalization capabilities, but mostly consider image uncertainty only during the rendering process. Although these methods have achieved good results, they still face challenges with artifacts and efficiency when applied to large-scale scenes.

Based on the above series of work, we model the radiance color at each sampling point in the scene as a Gaussian distribution to solve the above uncertainty references, which is used to assess rendering issues caused by unseen regions, including content outside the scene observed. For large-scale scene problems, inspired by oblique photography[24], we divide UAV flight paths into planar and non-planar trajectories[25, 26]. For these two different trajectories, we define a positional uncertainty to evaluate the positional gain provided by different 3D poses in real-world scenarios. We integrate rendering uncertainty and positional uncertainty as a novel standard metric hybrid uncertainty. We treat both with equal importance to determine the next best view that maximizes information gain.

Additionally, by selecting lightweight NeRF models, we fur-

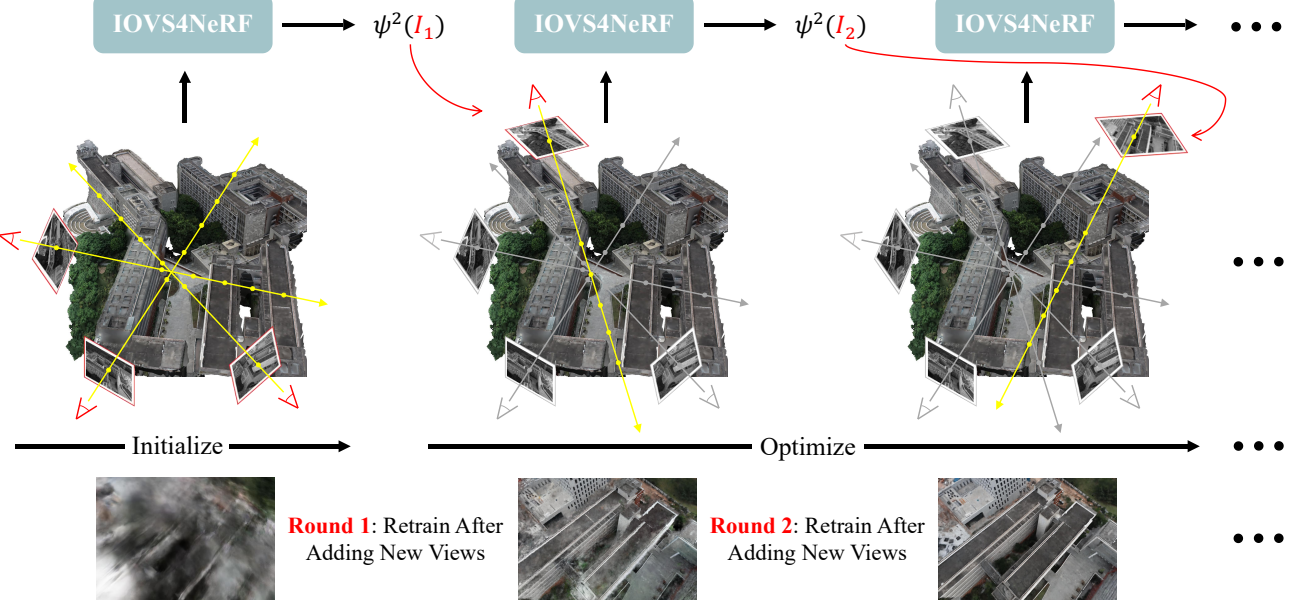


Fig. 2: **IOVS4NeRF** is a flexible framework that actively expands the existing training set with newly captured samples based on computed uncertainties of candidate views. IOVS4NeRF incorporates rendering uncertainty and the positional uncertainty of scene uncertainty at unobserved novel views. By selecting the view that brings the most information gain, the quality of novel view synthesis can be improved with minimal additional resources.

ther accelerate the reconstruction speed from the perspective of model structure. In this paper, we use Instant-NGP[9] as a tool to help us better reconstruct our scenes. Ultimately, we aim to achieve high-quality and high-efficiency NeRF reconstruction in large scenes with fewer computational resources. In summary, our contributions are as follows:

- We propose a NeRF framework for incremental optimal view selection, aiming at addressing the limitations of NeRFs in large-scale scenes with restrained computational cost.
- We define a novel estimation of uncertainty, which is comprised of rendering uncertainty and positional uncertainty, to compute the information gain of each candidate view.
- We extensively evaluate our method on real-world datasets, showing it significantly reduces time while maintaining reconstruction effectiveness compared to previous baselines.

## II. RELATED WORK

### A. Neural Radiance Fields

NeRF [1] is a high-quality scene reconstruction technique that combines 3D reconstruction with neural rendering technology. Its main task is novel view synthesis, which involves capturing a series of images from several known viewpoints and synthesizing images from unseen viewpoints. This method encodes a 3D scene as a radiance field represented by MLP. The network is used to learn the volumetric density and color of the 3D scene, optimizing the continuous volumetric scene and modeling it with high fidelity. Due to the encoding of scene information in the network parameters and the computation of differentiable volume rendering, NeRF's training and rendering processes consume substantial computational resources and time. As a result, many variations of the original

NeRF have emerged for efficient reconstruction [9, 10, 11, 12, 13]. Among these methods, Instant-NGP uses multiresolution hash encoding, which is adaptive and efficient. It not only accelerates training and conserves resources but also has good adaptability to scenes of different scales. Therefore, we chose to base our research on it in this paper.

### B. NeRFs for Large-Scale Scene

Due to the advantages of high-quality reconstruction offered by NeRF, various NeRF methods for large-scale scene reconstruction have emerged [14, 15, 16, 17]. Given the limited capacity of the original NeRF, which is unable to handle the vast data volumes in large-scale scenes, researchers have primarily adopted the idea of decomposing large scenes into several smaller ones, each with a corresponding NeRF module. Notable examples of NeRF methods that utilize scene partitioning include Mega-NeRF proposed by Turki et al. [15] and Block-NeRF proposed by Tancik et al. [16]. Mega-NeRF decomposes large-scale scenes captured by drones into multiple different spatial sub-scenes and uses a geometric clustering algorithm to divide the input images into different NeRF submodules that can be trained in parallel. Block-NeRF, on the other hand, divides large street scenes captured by vehicles into different small scene blocks, training each block in segments and fine-tuning them sequentially.

Datasets used for large-scale scene reconstruction often contain numerous images, which consume significant computational resources. Under resource constraints, reducing the number of dataset images can help decrease the computational load. However, applying these methods with fewer images directly often results in severe artifacts and lower visual

fidelity. The challenge that remains is how to ensure that the limited input data contains enough scene information, meaning all viewpoints are optimal, which is a critical problem that needs to be addressed.

### C. Uncertainty Estimation in NeRFs

NBV problem[18] aims to select the next viewpoint that maximizes information gain, enhancing scene understanding and minimizing uncertainty. Estimating uncertainty is key for NBV selection, but this remains a challenge in deep learning. Traditional methods like Bayesian Neural Networks (BNN)[27] require significant computational resources, limiting its use in extensive neural architectures. Deep Ensembles[28] need training multiple models and combining their predictions to estimate uncertainty, while MC-Dropout[29] relies on multiple forward passes during testing, leading to inefficiency.

Emerging works address NBV selection for NeRF training under constrained budgets. Some approaches modify NeRF's architecture, rendering, or training mechanisms, such as S-NeRF[30] and CF-NeRF[19], which use Bayesian methods to model radiance variance and density as random variables, estimating posterior distributions through variational inference. Active-NeRF[20] models radiance as a Gaussian distribution and minimizes negative log-likelihood to predict pixel uncertainty during training. Lee et al.[21] quantify scene uncertainty by calculating the density distribution along sampled rays. Another category of methods does not modify the NeRF architecture itself, making them applicable to any NeRF model. Niko et al.[23] estimate uncertainty via variance of ensemble predictions based on termination probability of rays intersecting unknown areas, while Kopanas et al.[31] introduce observation frequency and angular uniformity to assess camera placement uncertainty. Both methods are based on Instant-NGP. Our innovative approach combines rendering uncertainty in RGB space with spatial uncertainty of camera placement, proposing a hybrid uncertainty estimation for more effective NBV selection.

## III. BACKGROUND

In this section, we provide a brief overview of the NeRF framework and more details of this algorithm can be found in [1].

NeRF represents a scene as a continuous function  $F_\theta$  that outputs both the emitted radiance value and volume density. Specifically, given a 3D  $\mathbf{x} = (x, y, z)$  in the scene and a viewing direction vector  $\mathbf{d} = (\theta, \phi)$ , a multi-layer perceptron model is used to generate the corresponding volume density  $\sigma$  and color  $\mathbf{c} = (r, g, b)$  as follows:

$$[\sigma, f] = \text{MLP}_{\theta_1}(\gamma_x(\mathbf{x})), \quad (1)$$

$$\mathbf{c} = \text{MLP}_{\theta_2}(f, \gamma_d(\mathbf{d})), \quad (2)$$

where  $\gamma_x(\cdot)$  and  $\gamma_d(\cdot)$  are the positional encoding functions, and  $f$  represents the intermediate feature that is independent of the viewing direction  $\mathbf{d}$ . An interesting observation is that the

radiance color is influenced solely by its own 3D coordinates and the viewing direction, rendering it independent of other locations.

To enable free novel synthesis, NeRF utilizes volume rendering to determine the color of rays passing through the scene. Given a camera ray  $\mathbf{r}(t) = \mathbf{o} + t\mathbf{d}$  with the camera center  $\mathbf{o} \in \mathbb{R}^3$  passing through a specific pixel on the image plane, the color of the pixel can be expressed as:

$$C(\mathbf{r}) = \int_{t_n}^{t_f} T(t) \sigma(\mathbf{r}(t)) c(\mathbf{r}(t), \mathbf{d}) dt, \quad (3)$$

where  $T(t) = \exp\left(-\int_{t_n}^t \sigma(\mathbf{r}(s)) ds\right)$  denotes the accumulated transmittance, and  $t_n$  and  $t_f$  are the near and far bounds in the scene. To simplify the rendering process, NeRF approximates the integral using stratified sampling and represents it as a linear combination of sampled points:

$$\hat{C}(\mathbf{r}) = \sum_{i=1}^{N_s} \alpha_i c(\mathbf{r}(t_i)), \quad (4)$$

$$\alpha_i = \exp\left(-\sum_{j=1}^{i-1} \sigma_j \delta_j\right) (1 - \exp(-\sigma_i \delta_i)), \quad (5)$$

where  $\delta_i = t_{i+1} - t_i$  is the distance between adjacent samples, and  $N_s$  denotes the number of samples. Based on this approach, NeRF optimizes the continuous function  $F_\theta$  by minimizing the squared reconstruction errors between the ground truth RGB images  $\{I_{i=1}^N\}$  and the rendered pixel colors.

To enhance sampling efficiency, NeRF simultaneously optimizes two parallel networks, referred to as the coarse and fine models. The sampling strategy for the fine model is refined based on the results of the coarse model, with samples being biased towards more relevant regions. Overall, the optimization loss is parameterized as follows:

$$\sum_i \left\| C(\mathbf{r}_i) - \hat{C}^c(\mathbf{r}_i) \right\|_2^2 + \left\| C(\mathbf{r}_i) - \hat{C}^f(\mathbf{r}_i) \right\|_2^2, \quad (6)$$

where  $\mathbf{r}_i$  is a sampled ray, and  $C(\mathbf{r}_i), \hat{C}^c(\mathbf{r}_i), \hat{C}^f(\mathbf{r}_i)$  correspond to the ground truth, coarse model prediction, and fine model prediction respectively.

## IV. IOVS4NeRF

In this paper, we focus on optimal view selection for large-scale NeRFs. In this section, we present the *IOVS4NeRF* framework in section. IV-A followed by detailed descriptions of the proposed hybrid uncertainty estimation (section. IV-B) and implementation (section. IV-C).

### A. Framework

As shown in Fig. 3, the IOVS4NeRF framework consists of 3 steps. First, the random views are used to train for initialization. Then in every expansion round, we compute the uncertainties of each unused candidate view added to the one with the highest score into the training set until the quality of the synthesized novel view meets the requirement.

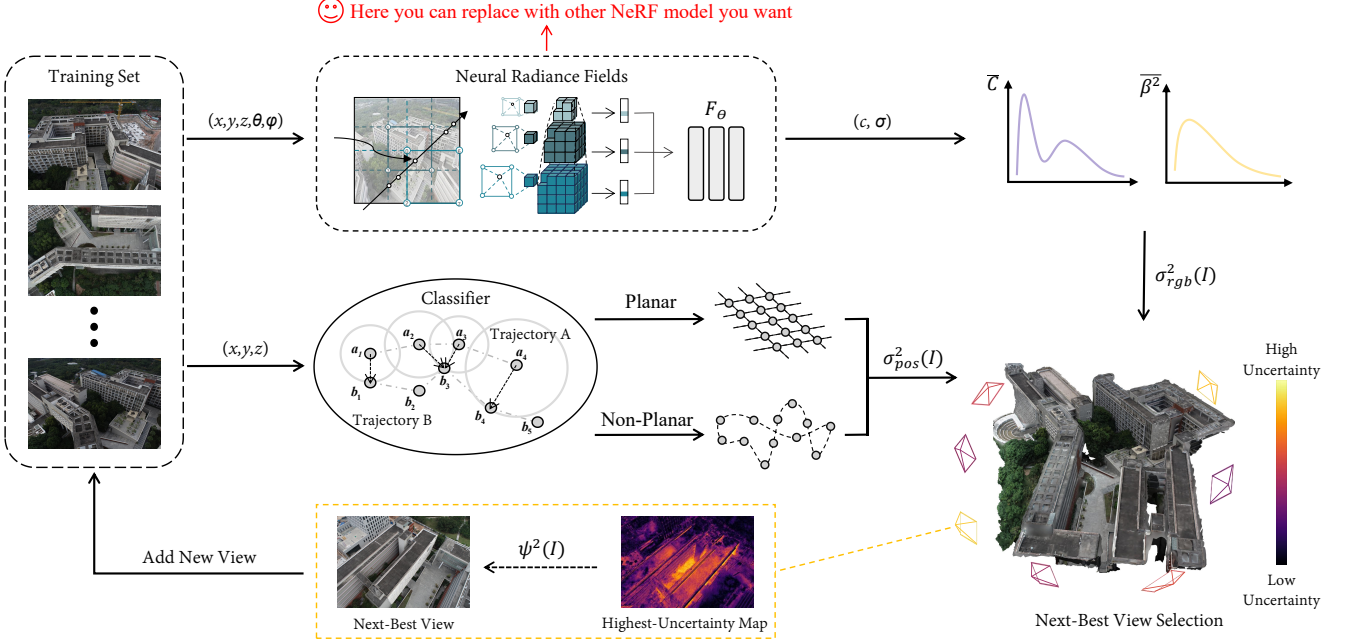


**Fig. 3: Overview of Our Framework.** It consists of three parts: I. Based on the 5D information of the images, we input them into NeRF for training. We define the color at a certain as a gaussian distribution and quantitatively obtain the mean and variance of color from the MLP, generating our rendering uncertainty. II. We extract the positional information of the images from the training set and input them into a classifier to determine their respective Voronoi positional uncertainty, resulting in hybrid uncertainty. III. Based on the hybrid information uncertainty, we select the images with the maximum gain from the candidate set and add them to the training set, iterating continuously.

**Initialization.** As shown in Fig. 2, we randomly select a fixed proportion of images (we experimentally recommend 15%) from the input dataset to perform NeRF training for initialization.

**Uncertainty Estimation.** Note that the IOVS4NeRF selects the best view based a novel information gain metric, named hybrid uncertainty, with two main terms: 1) rendering uncertainty and 2) positional uncertainty:

- For rendering uncertainty, we input 5D coordinates  $(\mathbf{x}, \mathbf{d})$  of the remaining photo set into a modified NeRF network with threshold sampling, which then outputs both color  $c$  and volume density  $\sigma$ , then it goes to opacity  $\alpha$  and the variance. Subsequently, we calculate the rendering uncertainty of the image by integrating both  $c$  and variance into a gaussian distribution.
- For positional uncertainty, we input 3D coordinates  $\mathbf{x}$  of the remaining photo set, and a classifier determines whether the trajectory is planar or non-planar. We then estimate the information using Voronoi diagrams to obtain the positional uncertainty.
- Then, we normalize and sum the two uncertainties to calculate the hybrid uncertainty, as shown in the following formula:

$$\psi^2(I) = \text{Norm}(\sigma_{pos}^2(I)) + \text{Norm}(\sigma_{rgb}^2(I)), \quad (7)$$

where  $I$  is the ground truth image while  $\text{Norm}(\cdot)$  is normalization function.  $\sigma_{rgb}^2(I)$  and  $\sigma_{pos}^2(I)$  are rendering and positional uncertainty respectively that defined in Eq. (12) and Eq. (18).

**Incremental Selection and Optimization.** We select the image with the highest hybrid uncertainty score and continually add it to the training set. This process is repeated until a specific reconstruction effect is achieved or a preset limit on the number of selected images is reached.

#### B. Hybrid Uncertainty Estimation

The proposed hybrid uncertainty (Eq. (7)) includes two terms, namely rendering uncertainty  $\sigma_{rgb}^2(I)$  and positional uncertainty  $\sigma_{pos}^2(I)$ . Note that our hybrid uncertainty is an epistemic uncertainty [27], which can be reduced by collecting more data.

**Rendering Uncertainty.** In scenarios with limited training data, the original NeRF framework often results in fragmented outputs due to predicting zero volume density for unobserved regions. To address this issue, we propose representing the RGB values at each scene as a gaussian distribution[20], rather than a single value. The predicted variance indicates the uncertainty at specific locations, allowing the model to assign larger variances to unobserved areas, thereby enhancing information gain for completing renderings and reducing epistemic uncertainty.

Specifically, we define the color at a certain as a gaussian distribution with parameters representing the mean  $c(\mathbf{r}(t_i))$  and variance  $\beta^2(\mathbf{r}(t_i))$ . We establish a variance model by adding an additional branch outside NeRF's MLP network using information entropy. The information entropy of each sampling point can be considered the variance of the color distribution at that point. This is because higher information

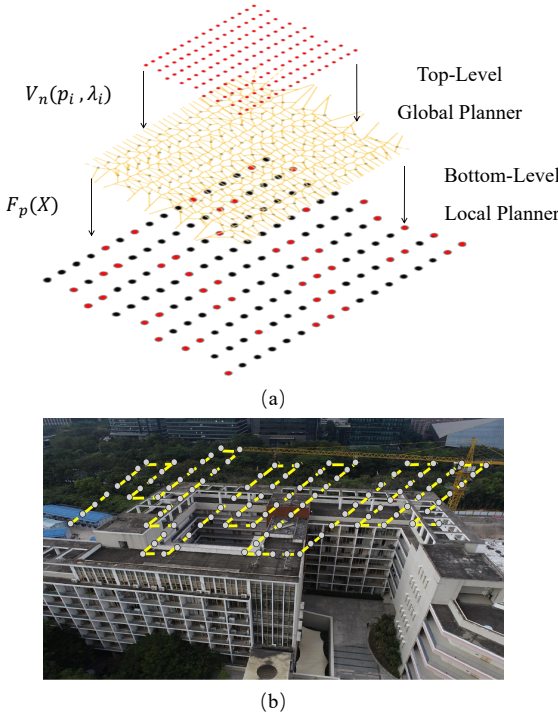


Fig. 4: For planar flight trajectories, we use Voronoi information radiation fields, with the top-level global planner employing a generalized Voronoi diagram to create and update a list of Voronoi nodes. The bottom-level local planner selects the largest node from the list based on the potential field formed by the weighted centroids, uploading it to the top level planner for further filtering.

entropy indicates more dispersed information distribution. It requires more information to describe, suggesting a greater difference between the predicted result and the true value, which aligns with the definition of variance:

$$\beta^2(\mathbf{r}(t_i)) = -P(\alpha_i) \log P(\alpha_i), \quad (8)$$

where  $\alpha_i$  is the same as Eq. (5), and  $P(\cdot)$  represents proportion of  $\alpha_i$  in the  $\sum \alpha_i$  along the ray.

During the rendering process, similar volume rendering methods can be used to handle new neural radiation fields with uncertainty. That is because volume rendering can be seen as a linear combination of sampled points along rays. And the volume density at a specific location is only affected by its 3D coordinates, not by the viewing direction  $\mathbf{d}$ , which makes the distributions at different  $\mathbf{s}$  independent of each other. Based on these conditions, if we represent the gaussian distribution at the  $\mathbf{r}(t_i)$  then, according to the conjugacy of the gaussian distribution, the rendering values along this ray naturally follow a gaussian distribution as:

$$\hat{C}(\mathbf{r}) \sim Beta(\bar{C}(\mathbf{r}), \bar{\beta}^2(\mathbf{r})), \quad (9)$$

where,

$$\bar{C}(\mathbf{r}) = \sum_{i=1}^{N_s} \alpha_i c(\mathbf{r}(t_i)), \quad (10)$$

$$\bar{\beta}^2(\mathbf{r}) = \sum_{i=1}^{N_s} \alpha_i^2 \beta^2(\mathbf{r}(t_i)), \quad (11)$$

and the  $\alpha_i$  is the same as in Eq. (5), and  $\bar{C}(\mathbf{r})$ ,  $\bar{\beta}^2(\mathbf{r})$  denote the mean and variance of the rendered color of the sampled point in the ray.

Assuming the distribution of the presented rays is independent, we can measure the information content of the viewpoint image by calculating the maximum log-likelihood of the rays from the same image. Therefore, our rendering uncertainty can be expressed as:

$$\sigma_{rgb}^2(I) = \sum_{i=1}^{N_r} \frac{\|C(\mathbf{r}_i) - \bar{C}(\mathbf{r}_i)\|_2^2}{2\bar{\beta}^2(\mathbf{r}_i)} + \frac{\log \bar{\beta}^2(\mathbf{r}_i)}{2}, \quad (12)$$

where  $N_r$  means the total number of the rays in photo  $I$ .

**Positional Uncertainty.** It has been determined that most drone flight paths that can be programmed follow an approximate planar trajectory, but users can freely manipulate the drone to fly along non planar trajectories. Therefore, it is necessary to consider the position distribution of drone trajectories.itemize

- **Planar Trajectories.** We employ a Voronoi-based information gain radiance field within a hierarchical planning framework. This framework comprises a superior planner that delineates local trajectory points utilizing Voronoi vertices, as per the methodology outlined in [32]. Concurrently, an inferior planner is tasked with the refinement of uncertainty biases, subsequently elevating these for consideration by the superior planner. The schematic representation of this process is depicted in Figure 4.

The top-level global planner uses an improved version of the generalized Voronoi diagram to form a graph of collision-free space. By traversing the nodes in the graph, the global planner creates and updates a list of Voronoi nodes, forming pose points that cover the maximum uncertainty. Then, the bottom-level local planner selects the largest node from the list based on the area potential field formed by weighted centroids and uploads it to the top-level planner for further filtering. This allows for adaptive exploration of uncertainty. Specifically, we compress 3D pose information points to two-dimensional Euclidean space and define  $p_i$  as  $n$  distinct points on this space, and  $\lambda_i$  as the weighted value of a given point. Then,  $V_n(p_i, \lambda_i)$  is the V-region of point  $p_i$  with weight  $\lambda_i$ , where  $d(p, p_i)$  is the Euclidean distance between  $p$  and  $p_i$ :

$$V_n(p_i, \lambda_i) = \bigcap_{j \neq i} \left\{ p \mid \frac{d(p, p_i)}{\lambda_i} < \frac{d(p, p_j)}{\lambda_j} \right\} \quad (13)$$

In a non-confusing context, we abbreviate  $V_n(p_i, \lambda_i)$  as  $V_n(p_i)$ . Based on this, the uncertainty of the information of our plane's Voronoi regions is defined as:

$$F_p(I) = \sum_{i=1}^{N_v} \frac{\sum_{j=1}^{N_v} \|p_i - p_j\|^{\lambda_i}}{A_i}, \quad (14)$$

where  $A_i$  represents area of the Voronoi polygon  $V_n(p_i)$ , and  $N_v$  means the total number of 3D pose points.

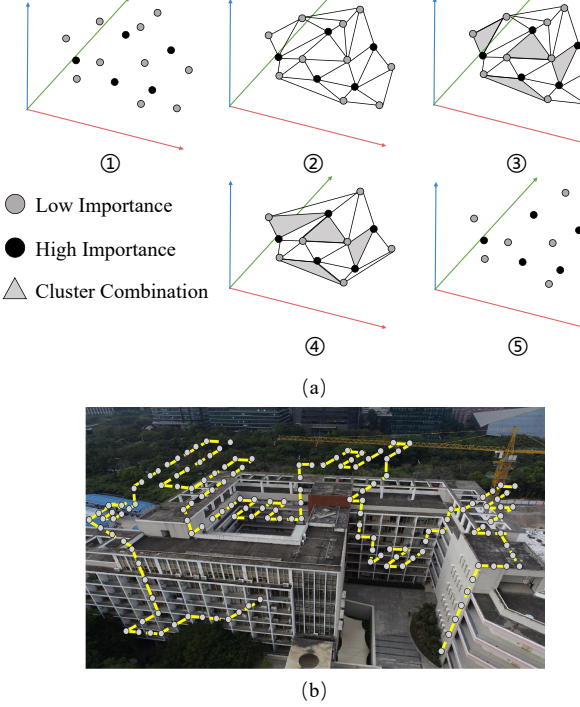


Fig. 5: For non-planar flight trajectories, we consider the maximum volume allowed by units that can be combined into evolving clusters. We approximate the local instance space density per unit volume, clustering each point and its neighbors in order of their sizes, and provide a quantifiable information uncertainty measure by combining importance values and relative local density.

• **Non-planar Flight Trajectories.** We employ the Voronoi clustering algorithm[33], which provides a threshold as an input parameter. This threshold represents the maximum volume allowed for units that can still be combined into evolving clusters. We approximate local instance space density through unit volume, making it important only when determining if the density is high enough to further combine into clusters, as shown in Fig. 5.

In the Voronoi diagram of the data, each point forms its own cell. Next, we approximate the volume of cells. In general, a cell has many neighboring cells with different class labels, and some cells are yet unmarked. Known neighbors are processed in order of their sizes. The considered cell is merged into the neighbor with the smallest class label, and its labeled neighbors also assume the same class. Cells are merged as long as the cell volume remains below the maximum value. After all points have been considered once, all cluster combinations have been executed. However, we still need to perform simple post-processing on the obtained clusters to make them reasonable.

The purpose of point cluster generalization is to correctly convey large-scale information into small-scale information diagrams, considering topological information, and metric information in the process. Based on this, we combine the concepts of importance value and relative local density with

the aforementioned cell cluster theory to evaluate the change in the importance value of the entire area and the importance value of the variation. The larger the area of the Voronoi polygon, the greater the weight. Thus, points are more likely to be retained in generalized mapping. The importance value equation is as followed:

$$G_i = \frac{\lambda_i A_i}{\sum_{k=1}^{N_v} (\lambda_k A_k)}, \quad (15)$$

where  $G_i$  is the probability of selecting the specific point and given by the product of the area of the Voronoi polygon, denoted as  $A_i$ , and the weight value, denoted as  $\lambda_i$ .

Relative local density enables the comparison of density changes point by point before and after generalization, thus better assessing the density changes between points before and after generalization. As follows:

$$r_i = \frac{\frac{1}{A_i}}{\sum_{k=1}^{N_v} \frac{1}{A_k}} \quad (16)$$

The information uncertainty of non-planer trajectory is:

$$F_{np}(I) = \sum_{i=1}^{N_v} -\log(G_i)r_i + \lambda_i \|G_i - r_i\|^2 \quad (17)$$

The all uncertainty can be expressed as:

$$\sigma_{pos}^2(I) = \mathbb{I}(p)F_p(I) + \mathbb{I}(np)F_{np}(I), \quad (18)$$

where  $\mathbb{I}(\cdot)$  represents the indicator function.

### C. Implementation

In this section, we introduce the implementation details of the proposed IOVS4NeRF.

**Proportionally Distributing Samples.** The first introduction is that we propose proportionally distributing samples for improved rendering effects while accelerating sampling based on a threshold. Specifically, we accelerate the process by accumulating transmittance along the ray and terminating sampling beyond a certain threshold.

**Trajectory Strategy Classifier.** We also design a classifier to determine whether the trajectory is planar or non. To implement our adaptive classifier, we divide the data point set into two groups,  $A = a_1, \dots, a_p$  and  $B = b_1, \dots, b_q$ , and measure the similarity between these two sets using the Hausdorff distance. Given two trajectories  $A = a_i$  and  $B = b_j$ , the Hausdorff distance between sets  $A$  and  $B$  is defined as:

$$H(A, B) = \max(h(A, B), h(B, A)), \quad (19)$$

where,

$$h(A, B) = \max(\min_{a_i \in A} \|a_i - b_j\|) \quad (20)$$

Compared to traditional distance measurement methods, the Hausdorff distance formula can directly calculate trajectory similarity without the need to interpolate the trajectory set, thereby avoiding the introduction of noise. By setting a fixed threshold, the nature of the flight trajectory can be determined.

If the Hausdorff distance between sets  $A$  and  $B$  exceeds the threshold, it indicates low similarity and the trajectory can be classified as non-planar; otherwise, it is considered planar.

**Solution Implementation.** As shown in Alg. 1 that the implementation of proposed IOVS4NeRF has four main steps:

- 1) Initialization for poses: We input the ground truth RGB images  $\{I_{i=1}^N\}$  into COLMAP, which is a software to recover the structures from images and output 3D  $\mathbf{x} = (x, y, z)$  in the scene and a viewing direction vector  $\mathbf{d} = (\theta, \phi)$ .
- 2) Initialization for NeRF: We randomly select a specific amount of images from dataset to train our weights of NeRF-MLP network. Through experiments, we recommend initializing with a quantity that is 15% of the total.
- 3) The usage of the variants of NeRFs: Chosing a lightweight NeRF model can further accelerate the reconstruction speed. Specifically, we apply Instant-NGP to the framework in our experiments.
- 4) The stop of our incremental selection: We choose to stop our workflow when a specific reconstruction effect is achieved or a preset limit on the number of selected images is reached.

---

**Algorithm 1** Hybrid Uncertainty Calculation Algorithm

---

- 1: **Input:** RGB ground truth photos  $\{I_{i=1}^N\}$
- 2: **Output:** hybrid uncertainty
- 3: Compute 3D  $\mathbf{x}$ , and viewing direction  $\mathbf{d}$  using COLMAP
- 4: Compute volume density  $\alpha_i$  and color  $c(\mathbf{r}(t_i))$  based on Eq. (5)
- 5: Compute variance  $\beta^2(\mathbf{r}(t_i))$  based on Eq. (8)
- 6: Construct Gaussian Distribution based on Eq. (9) and output  $\bar{C}(\mathbf{r})$ ,  $\bar{\beta}^2(\mathbf{r})$  based on Eq. (10), Eq. (11)
- 7: Compute rendering uncertainty  $\sigma_{rgb}^2$  using Eq. (12)
- 8: Compute Hausdorff distance based on Eq. (19)
- 9: **if**  $h(A, B) < \epsilon$  (a preset threshold) **then**
- 10:     Construct Voronoi diagram based on Eq. (13)
- 11:     Compute planar positional uncertainty based on Eq. (14)
- 12: **else**
- 13:     Construct Voronoi cell and its neighbors
- 14:     Compute importance value  $G_i$  based on Eq. (15)
- 15:     Compute reactive local density  $r_i$  based on Eq. (16)
- 16:     Compute non-planar positional uncertainty based on Eq. (17)
- 17: **end if**
- 18: Normalize and compute hybrid uncertainty based on Eq. (7)

---

## V. EXPERIMENTS

### A. Experimental Setup

**Datasets.** Our dataset comprises 7 groups: 2 from Mill-19, 2 from Urban-3D, one from Pix-4D, and 2 self-captured footage datasets from Changsha, Hunan.

We compare all the methods in the following publicly available large-scale datasets captured by UAVs:

- Mill19-Building: This dataset comprises 1920 images high resolution of  $4608 \times 3456$  pixels captured by UAVs within a  $0.125 \text{ km}^2$  area surrounding an industrial structure <sup>1</sup>.
- Mill19-Rubble: Rubble is a UAV imagery dataset containing 1678 images with  $4608 \times 3456$  pixel resolution <sup>2</sup>.
- Villa: Villa is a UAV photogrammetry dataset collected and released by Pixel4D, which includes 232 images with the resolution at  $6000 \times 4000$  pixels <sup>3</sup>.
- UrbanScene3D-Polytech and UrbanScene3D-Artsci: UrbanScene3D is a large-scale data platform for urban scene perception and reconstruction, encompassing over 128,000 high-resolution images across 16 scenes, covering a total area of 136 square kilometers <sup>4</sup>. Polytech and Artsci are subsets of UrbanScene3D, providing LiDAR scans and image sets. Specifically, polytech contains 798 UAV filmed images at  $4864 \times 3648$  pixels resolution while Artsci has 989 images at  $5472 \times 3648$  pixels resolution <sup>5</sup>.
- CSC-university and CSC-Lake: Both are self-collected UAV imagery datasets. CSC-university includes 391 images with resolution at  $4000 \times 3000$  pixels covering  $0.1 \text{ km}^2$ . While CSC-Lake contains 211 images with resolution at  $4000 \times 3000$  pixels covering  $0.9 \text{ km}^2$  <sup>6</sup>.

**Metrics.** Note that this work focuses on optimal view selection with hybrid uncertainty estimation. Thus, our evaluation metrics are divided into two types.

- 1) In the uncertainty estimation experiments, we evaluate the proposed against the existing works by comparing the prediction accuracy of uncertainty:
  - SRCC[34]: We use Spearman’s rank correlation coefficient (SRCC) to measure the monotonic relationship between average uncertainty estimation on test views and rendering errors.
  - AUSE[35]: We report the Area Under the Sparsification Error (AUSE) curve to evaluate structural similarity, which reveals the degree to which uncertainty matches rendering errors on pixels.
- 2) In novel view synthesis experiments, we evaluate the proposed against the existing works by comparing the following three metrics:
  - PSNR: Peak Signal-to-Noise Ratio (PSNR) is a classic metric for measuring image reconstruction quality.
  - SSIM[36]: Structural Similarity Index (SSIM) is a metric for measuring structural similarity between two images.
  - LPIPS[37]: Learned Perceptual Image Patch Similarity (LPIPS) is a learning-based metric that considers perceptual characteristics of the human visual system, which is widely used to measure perceptual differences between two images.

**Comparison Methods.** We applied the proposed solution, IOVS4NeRF, and three current popular methods designed to

<sup>1</sup><https://storage.cmusatyalab.org/mega-nerf-data/building-pixsfm.tgz/>

<sup>2</sup><https://storage.cmusatyalab.org/mega-nerf-data/rubble-pixsfm.tgz/>

<sup>3</sup><https://earldudley.com/products/pix4dmatic/>

<sup>4</sup><https://vcc.tech/UrbanScene3D/>

<sup>5</sup><https://vcc.tech/UrbanScene3D/>

<sup>6</sup>our dataset will come soon upon acceptance of the paper

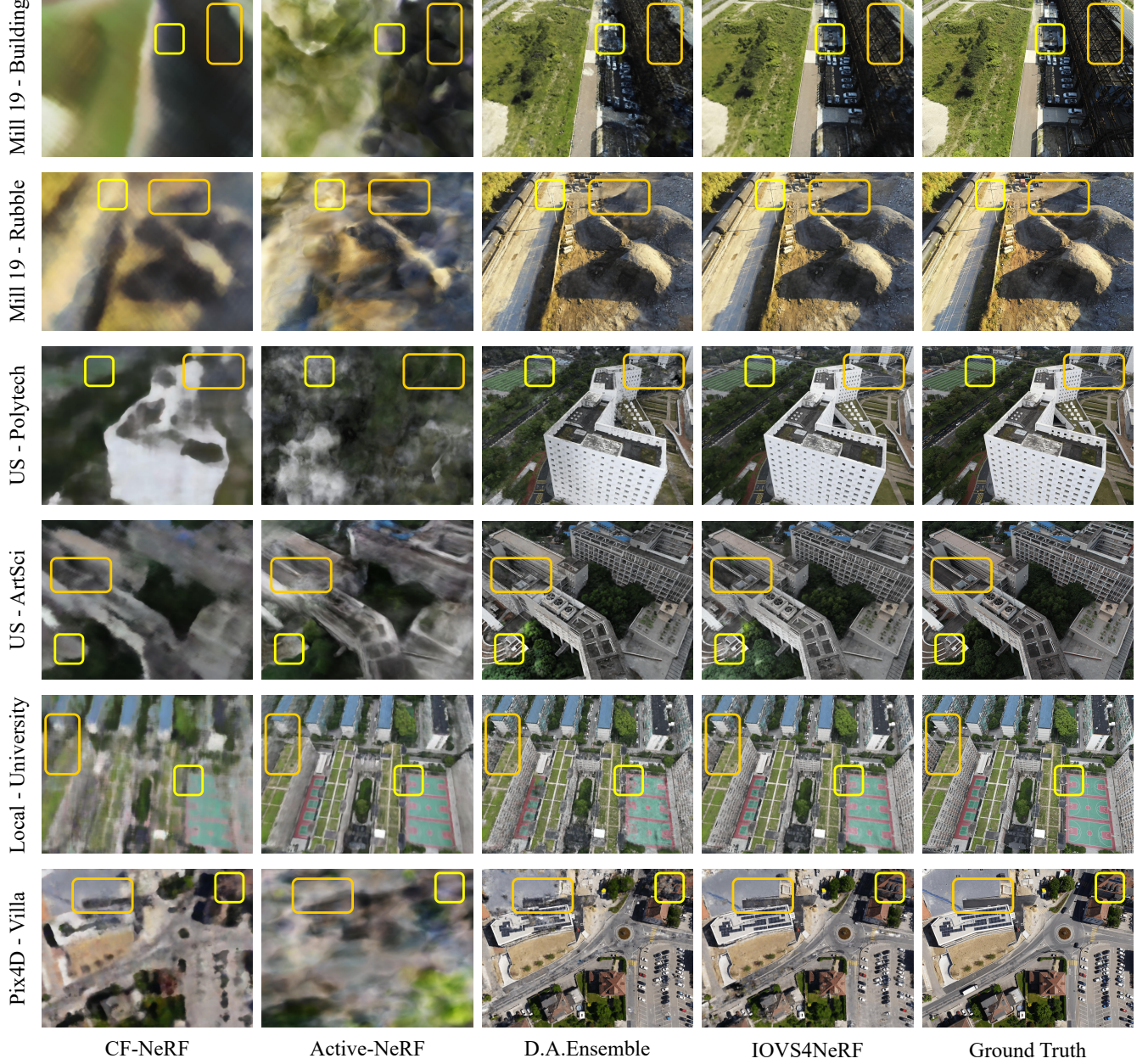


Fig. 6: Qualitative results on 6 realistic scenes. Several observations can be made: First, IOVS4NeRF performs significantly better than CF-NeRF and Active-NeRF. Also, IOVS4NeRF provides better synthesis quality among the objects with complex textures over *D.A.Ensemble* and are close to the ground truth.

exclusively estimate uncertainty in NeRF-based models to large-scale scenes for a comparison of reconstruction quality and computational consuming:

- CF-NeRF[19]<sup>7</sup>: CF-NeRF is a probabilistic framework that incorporates uncertainty quantification into NeRF by learning a distribution over all possible radiance fields, enabling reliable uncertainty estimation while maintaining model expressivity.
- Active-NeRF [20]<sup>8</sup>: ActiveNeRF is a learning framework

designed to model 3D scenes with a constrained input budget by incorporating uncertainty estimation into a NeRF model, ensuring robustness with few observations and providing scene interpretation.

- D.A.Ensemble[23]<sup>9</sup>: D.A.Ensemble quantifies model uncertainty in NeRF by incorporating a density-aware epistemic uncertainty term that considers termination probabilities along individual rays to identify uncertainty from unobserved parts of a scene, achieving SOTA perfor-

<sup>7</sup><https://github.com/poetrywanderer/CF-NeRF/>

<sup>8</sup><https://github.com/LeapLabTHU/ActiveNeRF/>

<sup>9</sup>no open resources released now, so we reproduce the code based on its paper

mance in uncertainty quantification benchmarks and supporting next-best view selection and model refinement.

**Setup Details.** We utilize the Instant-NGP [9] to demonstrate the effectiveness of the proposed IOVS4NeRF. All the experiments are conducted with a Intel core i9 CPU and an NVIDIA GeForce 3090 GPU (24GB memory).

TABLE I: Quantitative results in 6 real image scenes: IOVS4NeRF performs superior to or on par with the three state-of-the-art related solutions CF-NeRF, Active-NeRF and D.A.Ensemble in the quality of synthesized novel views (PSNR, SSIM and LPIPS), the accuracy of uncertainty estimation (AUSE and SRCC) and the efficiency (time-consuming). The best and second results are shown in **green** and **blue**, respectively.

Scenes	Methods	Quality Metrics			Uncertainty Metrics		Time↓
		PSNR↑	SSIM↑	LPIPS↓	AUSE↓	SRCC↑	
Building	CF-NeRF	14.926	0.260	0.738	<b>0.100</b>	<b>0.706</b>	12:57:17
	Active-NeRF	12.430	0.231	0.777	0.141	0.464	17:45:19
	D.A.Ensemble	<b>16.857</b>	<b>0.383</b>	<b>0.422</b>	0.303	0.668	<b>12:18:28</b>
	IOVS4NeRF	<b>19.841</b>	<b>0.469</b>	<b>0.351</b>	<b>0.055</b>	<b>0.878</b>	<b>7:28:20</b>
Rubble	CF-NeRF	17.758	0.312	0.717	<b>0.075</b>	<b>0.815</b>	12:58:39
	Active-NeRF	16.531	0.275	0.622	0.097	0.683	17:47:24
	D.A.Ensemble	<b>19.629</b>	<b>0.507</b>	<b>0.335</b>	0.257	<b>0.818</b>	<b>12:20:52</b>
	IOVS4NeRF	<b>21.108</b>	<b>0.573</b>	<b>0.303</b>	<b>0.052</b>	<b>0.884</b>	<b>7:29:14</b>
Polytech	CF-NeRF	14.259	0.251	0.731	0.118	<b>0.751</b>	12:57:28
	Active-NeRF	8.888	0.153	0.747	0.264	-0.035	17:46:55
	D.A.Ensemble	<b>20.673</b>	<b>0.564</b>	<b>0.253</b>	<b>0.058</b>	<b>0.915</b>	<b>12:46:18</b>
	IOVS4NeRF	<b>21.810</b>	<b>0.592</b>	<b>0.235</b>	<b>0.053</b>	<b>0.925</b>	<b>7:48:22</b>
ArtSci	CF-NeRF	15.578	0.227	0.693	<b>0.106</b>	0.729	12:57:14
	Active-NeRF	13.531	0.193	0.610	0.152	0.525	17:48:20
	D.A.Ensemble	<b>17.769</b>	<b>0.463</b>	<b>0.338</b>	0.101	<b>0.793</b>	13:28:42
	IOVS4NeRF	<b>18.836</b>	<b>0.500</b>	<b>0.319</b>	<b>0.083</b>	<b>0.834</b>	<b>8:21:14</b>
University	CF-NeRF	15.359	0.189	0.669	<b>0.112</b>	0.645	12:58:12
	Active-NeRF	<b>17.814</b>	<b>0.359</b>	<b>0.359</b>	0.087	<b>0.780</b>	17:46:50
	D.A.Ensemble	16.610	0.331	0.416	0.101	0.682	<b>12:08:12</b>
	IOVS4NeRF	<b>18.722</b>	<b>0.430</b>	<b>0.327</b>	<b>0.077</b>	<b>0.814</b>	<b>6:47:53</b>
Villa	CF-NeRF	15.141	0.259	0.645	<b>0.111</b>	<b>0.777</b>	<b>12:58:44</b>
	Active-NeRF	9.236	0.121	0.828	0.242	0.055	20:32:57
	D.A.Ensemble	<b>15.415</b>	<b>0.337</b>	<b>0.494</b>	0.123	0.689	13:58:26
	IOVS4NeRF	<b>18.250</b>	<b>0.457</b>	<b>0.386</b>	<b>0.079</b>	<b>0.868</b>	<b>8:46:40</b>

## B. Evaluation of Uncertainty Estimation

Our first experiment is to demonstrate that our uncertainty estimation strongly correlates with novel view synthesis quality for NeRFs. To evaluate the quality of uncertainty prediction, we consider two metrics, namely, SRCC and AUSE, that are widely used in existing next-best view selection solution [22].

For each dataset, we generate 100 test sets. Each set contains four randomly selected images from the scene, with three used as reference images and the fourth as the test view. We calculate the average predicted uncertainty and mean squared error (MSE) for each test view. Subsequently, we determine the SRCC values for the 100 pairs of averaged uncertainty and MSE. SRCC values above 0.8 empirically indicate a strong monotonic relationship (higher average uncertainty predictions correspond to higher average rendering errors). Additionally,

we report the average AUSE across 100 test views for each scene. An AUSE of 0 signifies that the pixel-wise uncertainty magnitudes are perfectly aligned with the MSE values (uncertain areas in the rendered test view coincide with erroneous predictions).

We compare IOVS4NeRF against the SOTA of NeRF-Based view selection solutions. As shown in Table. I, IOVS4NeRF achieves significant more information in uncertainty prediction with respect to synthesis error over CF-NeRF, Active-NeRF and D.A.Ensemble. The superior performance of our the approach demonstrates the proposed hybrid uncertainty leads to more consistent uncertainty estimates compared to solely rendering-based uncertainty such as CF-NeRF, Active-NeRF, and D.A.Ensemble.

## C. Evaluation of Novel View Synthesis

In this section, we evaluate the proposed method via the quality of novel view synthesis. Specifically, we compare IOVS4NeRF against optimal view selection baselines and state-of-the-art solutions.

For each dataset, due to GPU limitations, we randomly select 500 images as the full image set (if the total number of image in a dataset is less than 500, we use all the images instead). We randomly choose 15% of the images in each dataset for initialization and randomly select 10% of the images as the test set. Then we incrementally select 15% of the images using various view selection methods as the optimal views for incremental training. Thus, only 30% of the full image set are used to synthesis the novel view, of which quality are evaluated by using PSNR, SSIM and LPIPS.

## Comparison of Baseline Optimal View Selection Strategies.

We compare the proposed optimal view selection approach IOV4NeRF against two heuristic baselines:

- Random: We select a view candidate uniformly at random.
- FVS: We select the view that maximizes the view distance with respect to previously collected images.

As shown in Fig. 7, the rendering quality (PSNR score) of the ArtSci dataset by all three methods keeps growing with the increasing number of selected views. However, the PSNR of IOVS4NeRF raises significantly faster over FVS and Random which indicates that our approach is capable of selecting informative views.

As shown in Table. II that IOVS4NeRF outperforms FVS and Random in PSNR, SSIM and LPIPS by a significant margin, with the rendering quality close to the results trained with the full image sets. The quantitative results in Table. II also verify the effectiveness of the proposed IOVS4NeRF over the baseline strategies.

## Comparison of State-of-the-art Optimal View Selection.

We validate the performance of our proposed framework, IOVS4NeRF, and compare it with three state-of-the-art NeRF-based optimal view selection solutions, namely, CF-NeRF, Active-NeRF and D.A.Ensemble.

TABLE II: Quantitative comparison of IOVS4NeRF against to two baselined view selection strategies Random and FVS on the ArtSci dataset. We report the average PSNR, SSIM and LPIPS scores of the synthesized novel views by using the incremental select 15% images. Note that only 30% of the full image set is used for IOVS4NeRF, Random and FVS. Our proposed approach IOVS4NeRF finds informative images in the scene, and provides the best performance. The best and second results are shown in **green** and **blue**, respectively.

Method \ Scene	Building	Rubble	Polytech	ArtSci	Villa	University
Random	PSNR↑ 16.857	18.959	20.245	17.281	14.547	16.093
	SSIM↑ 0.383	0.500	0.554	0.444	0.307	0.305
	LPIPS↓ 0.422	0.330	0.266	0.348	0.527	0.447
FVS	PSNR↑ 17.272	20.045	18.606	17.687	15.917	16.338
	SSIM↑ 0.368	0.491	0.534	0.451	0.360	0.305
	LPIPS↓ 0.428	0.341	0.283	0.352	0.475	0.443
Ours	PSNR↑ <b>19.841</b>	<b>21.108</b>	<b>21.810</b>	<b>18.836</b>	<b>18.250</b>	<b>18.722</b>
	SSIM↑ <b>0.469</b>	<b>0.573</b>	<b>0.592</b>	<b>0.500</b>	<b>0.457</b>	<b>0.430</b>
	LPIPS↓ <b>0.351</b>	<b>0.303</b>	<b>0.265</b>	<b>0.319</b>	<b>0.386</b>	<b>0.327</b>
Full	PSNR↑ <b>20.547</b>	<b>22.613</b>	<b>22.661</b>	<b>19.408</b>	<b>19.509</b>	<b>19.666</b>
	SSIM↑ <b>0.525</b>	<b>0.592</b>	<b>0.619</b>	<b>0.538</b>	<b>0.485</b>	<b>0.463</b>
	LPIPS↓ <b>0.319</b>	<b>0.265</b>	<b>0.220</b>	<b>0.306</b>	<b>0.387</b>	<b>0.322</b>

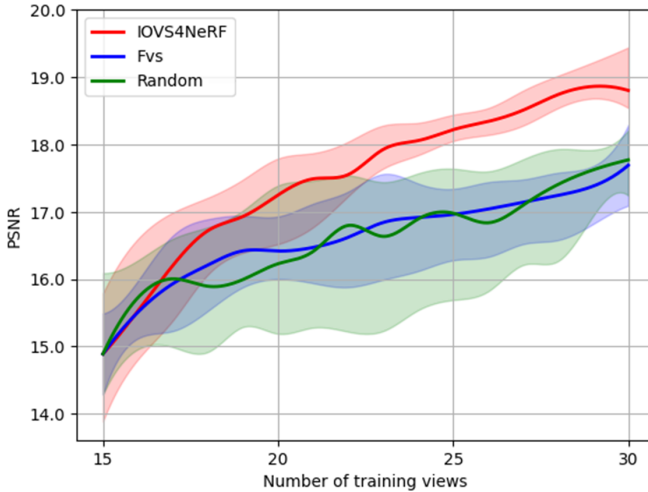


Fig. 7: Comparison of IOVS4NeRF against to two baselined view selection strategies Random and FVS on the ArtSci dataset. For each test scene, we incrementally retrain the instant-NGP model by adding the new views selected by IOVS4NeRF, Random and FVS at each step, then render tested views and report the average PSNR scores with standard deviations over all test scenes and runs respectively. Note that the large standard deviations are due to the varying rendering difficulty of each scene. Our proposed approach IOVS4NeRF finds informative images in the scene, improving scene representations via image-based neural rendering.

We first show the results with an incremental learning scheme, where the time and computation resources are considered sufficient. As shown in Figure. 6, we can easily see that IOVS4NeRF generate better visual quality synthesized novel views against the outputs of CF-NeRF, Active-NeRF and D.A.Ensemble, that are closed to the ground truth among all 6 datasets. The quantitative results in Table. I also show IOVS4NeRF achieves the best performance in three synthesis

image quality evaluation metrics (PSNR, SSIM, LPIPS) over the CF-NeRF, Active-NeRF and D.A.Ensemble. These experimental observations prove the proposed method IOVS4NeRF can select most informative inputs compared with state-of-the-art approaches, which contributes most to synthesizing views from less observed regions.

The runtime comparison in Table. I shows that IOVS4NeRF outperforms CF-NeRF, Active-NeRF and D.A.Ensemble in efficiency with a significant margin. We interpret this acceleration mainly due to that all three compared optimal view selection strategies in CF-NeRF, Active-NeRF and D.A.Ensemble are hard-coded with a NeRF module while IOVS4NeRF is a flexible framework where the proposed hybrid uncertainty computation is as a plug-in to any NeRF solution (e.g. Instant-NGP in our experiment). This soft-coded scheme leads to an advantage in efficiency. It is vital to notice that once a more advanced NeRF solution be developed in the future, it can be easily applied in IOVS4NeRF and is supposed to achieve further improvements in both synthesize quality and time-consuming.

#### D. Ablation Study

Note that in this paper, we propose to use hybrid uncertainty over the solely rendering uncertainty that is widely used in existing works. Thus, in this experiment, we further evaluate the effectiveness of the candidate uncertainty estimation module alone. We denote the baseline approaches as:

- w/o  $\sigma_{pos}^2$ : IOVS4NeRF with rendering uncertainty  $\sigma_{rgb}^2$  only by removing the positional uncertainty term  $\sigma_{pos}^2$  in Eq. (7).
- w/o  $\sigma_{rgb}^2$ : IOVS4NeRF with positional uncertainty  $\sigma_{pos}^2$  only by removing the rendering uncertainty term  $\sigma_{rgb}^2$  in Eq. (7).
- Full Model: IOVS4NeRF with completed hybrid uncertainty computation strategy shown in Eq. (7).

The quantitative experimental results are shown in Table. III while the qualitative experimental results are shown in Figure. 8. Both comparisons show that IOVS4NeRF obviously

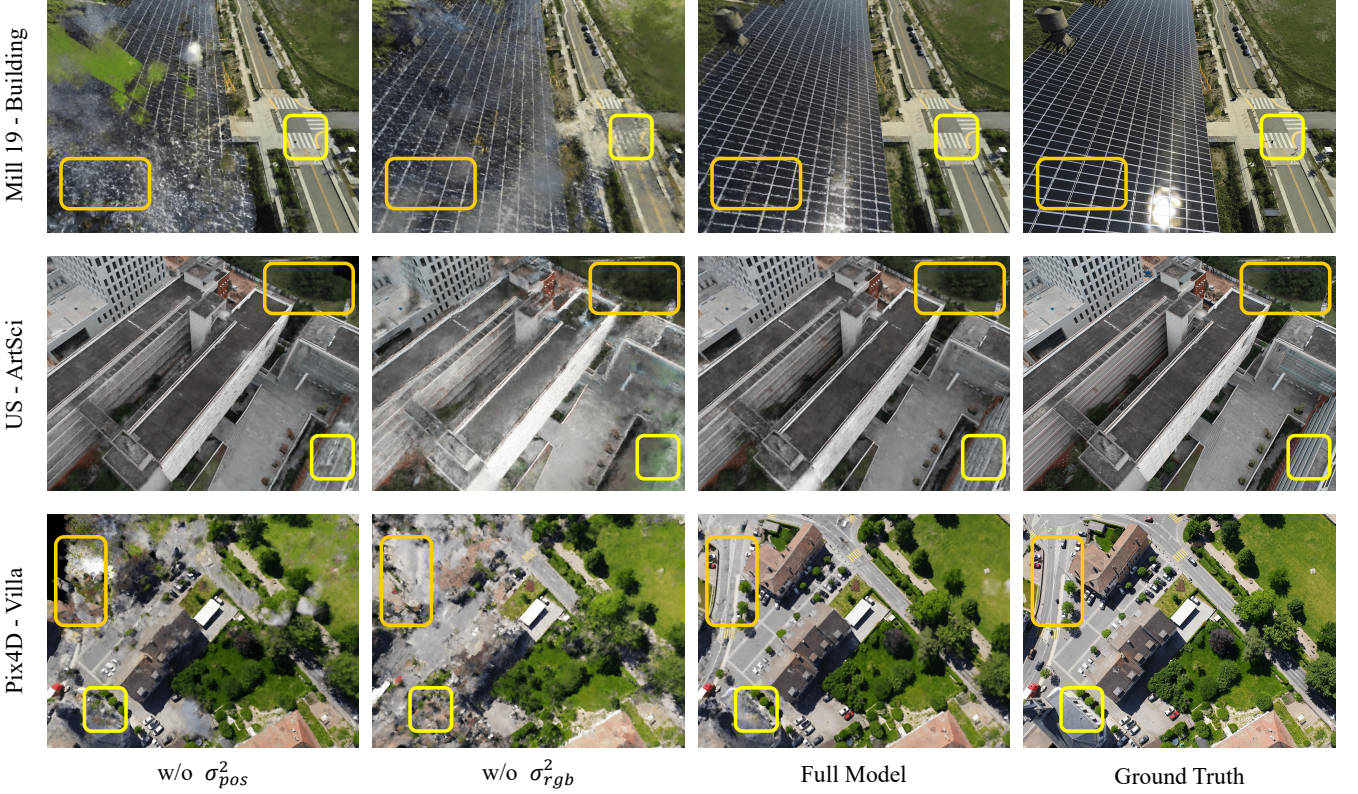


Fig. 8: Qualitative comparisons in ablation study by removing the rendering uncertainty  $\sigma_{rgb}^2$  and positional uncertainty  $\sigma_{pos}^2$  in proposed hybrid uncertainty one by one.

TABLE III: Ablation on hybrid uncertainty by removing the rendering uncertainty  $\sigma_{rgb}^2$  and positional uncertainty  $\sigma_{pos}^2$  one by one. The best and second results are shown in green and blue, respectively.

Component \ Scene	Building	Rubble	Polytech	ArtSci	Villa	University
w/o $\sigma_{pos}^2$	PSNR↑ 17.031	19.803	<b>19.856</b>	<b>18.386</b>	<b>15.937</b>	<b>16.782</b>
	SSIM↑ <b>0.404</b>	<b>0.527</b>	<b>0.541</b>	<b>0.497</b>	0.356	0.329
	LPIPS↓ <b>0.407</b>	0.645	0.731	0.693	0.645	0.669
w/o $\sigma_{rgb}^2$	PSNR↑ <b>17.841</b>	<b>20.045</b>	18.606	17.687	15.917	16.338
	SSIM↑ 0.390	0.491	0.534	0.451	<b>0.368</b>	0.305
	LPIPS↓ 0.421	<b>0.341</b>	0.534	<b>0.352</b>	<b>0.475</b>	<b>0.443</b>
Full Model	PSNR↑ <b>19.841</b>	<b>21.108</b>	<b>21.810</b>	18.836	<b>18.250</b>	<b>18.722</b>
	SSIM↑ <b>0.469</b>	<b>0.573</b>	<b>0.592</b>	<b>0.500</b>	<b>0.457</b>	<b>0.430</b>
	LPIPS↓ <b>0.351</b>	<b>0.303</b>	<b>0.235</b>	0.319	0.386	0.327

outperforms ablated approaches consistently which indicates that both rendering uncertainty  $\sigma_{rgb}^2$  and positional uncertainty  $\sigma_{pos}^2$  contributes to the uncertainty estimation of the candidate view and improve the capability of informative view selection.

#### E. Benefit to Classical Photogrammetry Solutions

Note that the proposed approach IOVS4NeRF is a flexible framework to assist NeRF-based novel view synthesis. It is interesting if IOVS4NeRF can assist the classical photogrammetry pipeline. In this experiment, we use the selected views by IOVS4NeRF, Random, FVS and completed image set Full as input to famous commercial photogrammetry software MetaShape to perform the dense 3D reconstruction pipeline for comparison. Specifically, we randomly 25% images in

Lake and Polytech datasets as initialization and select 25% views in the rest set by using IOVS4NeRF, Random, FVS for incrementally re-training. The results in Figure. 9 show that the reconstructed scenes by using the selected views from Random, FVS are with obvious artifacts. In contrast, the selected views by IOVS4NeRF lead to similar 3D reconstruction quality as the ones using Full image sets as input for MetaShape but with only half processing time. This experiment demonstrates IOVS4NeRF not only can ameliorate the novel view synthesis task by using NeRFs, but also benefit the classical photogrammetry solutions.

## VI. CONCLUSION

In conclusion, this study introduces IOVS4NeRF, an incremental optimal view selection framework aimed at addressing

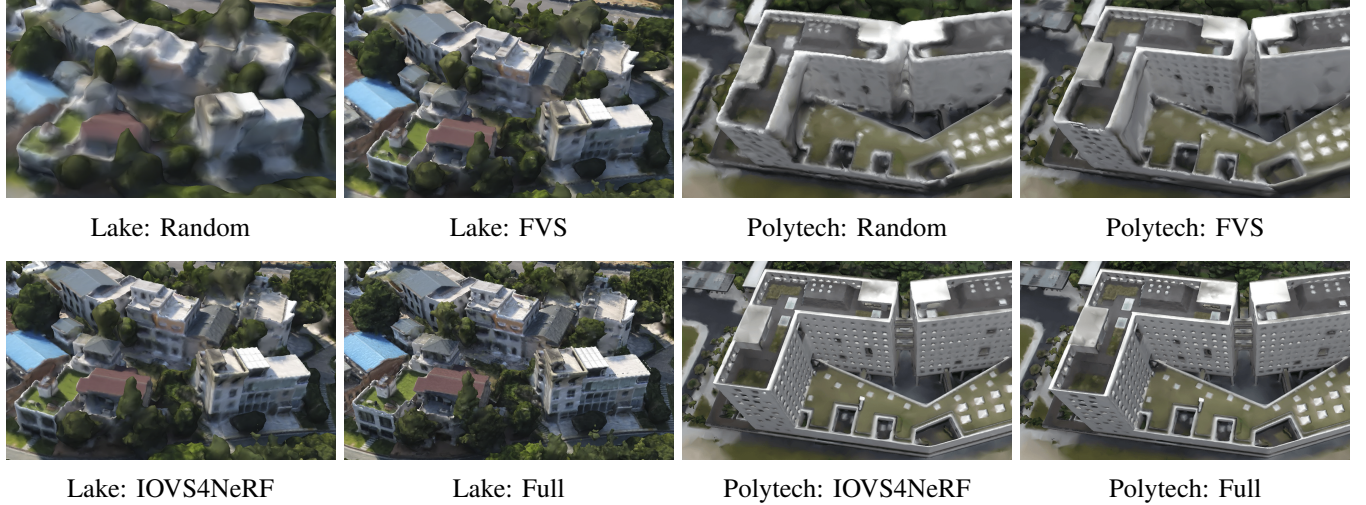


Fig. 9: Verification of the capability of the proposed method IOVS4NeRF to benefit classical photogrammetry. Several observations can be made: the selected views by IOVS4NeRF lead to similar 3D reconstruction quality as the ones using *Full* image sets as input for MetaShape but with only half processing time.

the limitations of NeRF in resource-constrained scenarios. By actively expanding the training dataset with strategically selected samples based on a novel hybrid uncertainty metric, IOVS4NeRF significantly enhances the quality of novel view synthesis while minimizing additional resource requirements. The efficacy of this approach has been validated through extensive experiments on realistic scenes, demonstrating its robustness even with limited training data. Future work will focus on further refining the model and exploring its applicability in various real-world scenarios. The implementation code will be released following the paper's acceptance, facilitating further research and development in this domain.

## VII. ACKNOWLEDGEMENT

This project is supported by Provincial Natural Science Foundation of Hunan(2024JJ10027) .

## REFERENCES

- [1] B. Mildenhall, P. P. Srinivasan, M. Tancik, J. T. Barron, R. Ramamoorthi, and R. Ng, “Nerf: Representing scenes as neural radiance fields for view synthesis,” *Communications of the ACM*, vol. 65, no. 1, pp. 99–106, 2021.
- [2] J. T. S. Phang, K. H. Lim, and R. C. W. Chiong, “A review of three dimensional reconstruction techniques,” *Multimedia Tools and Applications*, vol. 80, no. 12, pp. 17 879–17 891, 2021.
- [3] C. B. Choy, D. Xu, J. Gwak, K. Chen, and S. Savarese, “3d-r2n2: A unified approach for single and multi-view 3d object reconstruction,” in *Computer Vision-ECCV 2016: 14th European Conference, Amsterdam, The Netherlands, October 11-14, 2016, Proceedings, Part VIII 14*. Springer, 2016, pp. 628–644.
- [4] N. Wang, Y. Zhang, Z. Li, Y. Fu, W. Liu, and Y.-G. Jiang, “Pixel2mesh: Generating 3d mesh models from single rgb images,” in *Proceedings of the European conference on computer vision (ECCV)*, 2018, pp. 52–67.
- [5] H. Fan, H. Su, and L. J. Guibas, “A point set generation network for 3d object reconstruction from a single image,” in *Proceedings of the IEEE conference on computer vision and pattern recognition*, 2017, pp. 605–613.
- [6] R. Chen, S. Han, J. Xu, and H. Su, “Point-based multi-view stereo network,” in *Proceedings of the IEEE/CVF international conference on computer vision*, 2019, pp. 1538–1547.
- [7] R. Ranjan, S. Sankaranarayanan, A. Bansal, N. Bodla, J.-C. Chen, V. M. Patel, C. D. Castillo, and R. Chellappa, “Deep learning for understanding faces: Machines may be just as good, or better, than humans,” *IEEE Signal Processing Magazine*, vol. 35, no. 1, pp. 66–83, 2018.
- [8] A. Yu, V. Ye, M. Tancik, and A. Kanazawa, “pixelnerf: Neural radiance fields from one or few images,” in *Proceedings of the IEEE/CVF Conference on Computer Vision and Pattern Recognition*, 2021, pp. 4578–4587.
- [9] T. M”uller, A. Evans, C. Schied, and A. Keller, “Instant neural graphics primitives with a multiresolution hash encoding,” *ACM Transactions on Graphics (ToG)*, vol. 41, no. 4, pp. 1–15, 2022.
- [10] A. Chen, Z. Xu, A. Geiger, J. Yu, and H. Su, “Tensorf: Tensorial radiance fields,” in *European conference on computer vision*. Springer, 2022, pp. 333–350.
- [11] S. Fridovich-Keil, A. Yu, M. Tancik, Q. Chen, B. Recht, and A. Kanazawa, “Plenoxels: Radiance fields without neural networks,” in *Proceedings of the IEEE/CVF conference on computer vision and pattern recognition*, 2022, pp. 5501–5510.
- [12] C. Sun, M. Sun, and H.-T. Chen, “Direct voxel grid optimization: Super-fast convergence for radiance fields reconstruction,” in *Proceedings of the IEEE/CVF conference on computer vision and pattern recognition*, 2022, pp. 5459–5469.
- [13] Q. Xu, Z. Xu, J. Philip, S. Bi, Z. Shu, K. Sunkavalli, and U. Neumann, “Point-nerf: Point-based neural radiance fields,” in *Proceedings of the IEEE/CVF conference on computer vision and pattern recognition*, 2022, pp. 5438–5448.
- [14] Y. Xiangli, L. Xu, X. Pan, N. Zhao, A. Rao, C. Theobalt, B. Dai, and D. Lin, “Bungeenerf: Progressive neural radiance field for extreme multi-scale scene rendering,” in *European conference on computer vision*. Springer, 2022, pp. 106–122.
- [15] H. Turki, D. Ramanan, and M. Satyanarayanan, “Mega-nerf: Scalable construction of large-scale nerfs for virtual fly-throughs,” in *Proceedings of the IEEE/CVF Conference on Computer Vision and Pattern Recognition*, 2022, pp. 12 922–12 931.
- [16] M. Tancik, V. Casser, X. Yan, S. Pradhan, B. Mildenhall, P. P. Srinivasan, J. T. Barron, and H. Kretzschmar, “Block-nerf: Scalable large scene neural view synthesis,” in *Proceedings of the IEEE/CVF Conference on Computer Vision and Pattern Recognition*, 2022, pp. 12 922–12 931.

*Recognition*, 2022, pp. 8248–8258.

[17] M. Zhenxing and D. Xu, “Switch-nerf: Learning scene decomposition with mixture of experts for large-scale neural radiance fields,” in *The Eleventh International Conference on Learning Representations*, 2022.

[18] R. Zeng, Y. Wen, W. Zhao, and Y.-J. Liu, “View planning in robot active vision: A survey of systems, algorithms, and applications,” *Computational Visual Media*, vol. 6, pp. 225–245, 2020.

[19] J. Shen, A. Agudo, F. Moreno-Noguer, and A. Ruiz, “Conditional-flow nerf: Accurate 3d modelling with reliable uncertainty quantification,” in *European Conference on Computer Vision*. Springer, 2022, pp. 540–557.

[20] X. Pan, Z. Lai, S. Song, and G. Huang, “Activenerf: Learning where to see with uncertainty estimation,” in *European Conference on Computer Vision*. Springer, 2022, pp. 230–246.

[21] S. Lee, L. Chen, J. Wang, A. Liniger, S. Kumar, and F. Yu, “Uncertainty guided policy for active robotic 3d reconstruction using neural radiance fields,” *IEEE Robotics and Automation Letters*, vol. 7, no. 4, pp. 12 070–12 077, 2022.

[22] L. Jin, X. Chen, J. Ruckin, and M. Popović, “Neu-nbv: Next best view planning using uncertainty estimation in image-based neural rendering,” *arXiv preprint arXiv:2303.01284*, 2023.

[23] N. Sünderhauf, J. Abou-Chakra, and D. Miller, “Density-aware nerf ensembles: Quantifying predictive uncertainty in neural radiance fields,” in *2023 IEEE International Conference on Robotics and Automation (ICRA)*. IEEE, 2023, pp. 9370–9376.

[24] T. Zhou, L. Lv, J. Liu, and J. Wan, “Application of uav oblique photography in real scene 3d modeling,” *The International Archives of the Photogrammetry, Remote Sensing and Spatial Information Sciences*, vol. 43, pp. 413–418, 2021.

[25] M. Roberts, D. Dey, A. Truong, S. Sinha, S. Shah, A. Kapoor, P. Hanrahan, and N. Joshi, “Submodular trajectory optimization for aerial 3d scanning,” in *Proceedings of the IEEE International Conference on Computer Vision*, 2017, pp. 5324–5333.

[26] G. Petrie, “Systematic oblique aerial photography using multiple digital cameras,” *Photogrammetric Engineering & Remote Sensing*, vol. 75, no. 2, pp. 102–107, 2009.

[27] A. Kendall and Y. Gal, “What uncertainties do we need in bayesian deep learning for computer vision?” *Advances in neural information processing systems*, vol. 30, 2017.

[28] B. Lakshminarayanan, A. Pritzel, and C. Blundell, “Simple and scalable predictive uncertainty estimation using deep ensembles,” *Advances in neural information processing systems*, vol. 30, 2017.

[29] Y. Gal and Z. Ghahramani, “Dropout as a bayesian approximation: Representing model uncertainty in deep learning,” in *international conference on machine learning*. PMLR, 2016, pp. 1050–1059.

[30] J. Shen, A. Ruiz, A. Agudo, and F. Moreno-Noguer, “Stochastic neural radiance fields: Quantifying uncertainty in implicit 3d representations,” in *2021 International Conference on 3D Vision (3DV)*. IEEE, 2021, pp. 972–981.

[31] G. Kopanas and G. Drettakis, “Improving nerf quality by progressive camera placement for unrestricted navigation in complex environments,” *arXiv preprint arXiv:2309.00014*, 2023.

[32] K. Ok, S. Ansari, B. Gallagher, W. Sica, F. Dellaert, and M. Stilman, “Path planning with uncertainty: Voronoi uncertainty fields,” in *2013 IEEE International Conference on Robotics and Automation*. IEEE, 2013, pp. 4596–4601.

[33] H. Yan and R. Weibel, “An algorithm for point cluster generalization based on the voronoi diagram,” *Computers & Geosciences*, vol. 34, no. 8, pp. 939–954, 2008.

[34] C. Spearman, “The proof and measurement of association between two things.” 1961.

[35] E. Ilg, O. Cicek, S. Galesso, A. Klein, O. Makansi, F. Hutter, and T. Brox, “Uncertainty estimates and multi-hypotheses networks for optical flow,” in *Proceedings of the European Conference on Computer Vision (ECCV)*, 2018, pp. 652–667.

[36] Z. Wang, A. C. Bovik, H. R. Sheikh, and E. P. Simoncelli, “Image quality assessment: from error visibility to structural similarity,” *IEEE transactions on image processing*, vol. 13, no. 4, pp. 600–612, 2004.

[37] R. Zhang, P. Isola, A. A. Efros, E. Shechtman, and O. Wang, “The unreasonable effectiveness of deep features as a perceptual metric,” in *Proceedings of the IEEE conference on computer vision and pattern recognition*, 2018, pp. 586–595.